Archives of Acoustics Vol. 51, No. 1, pp. 145–159 (2026), https://doi.org/10.24423/archacoust.2026.4275

Research Paper

Study on Dual-Stage Amplification Cascaded Piezoelectric Transducer for High-Power Applications

Guo Li[(1)]*, Peiyu Tan[(1)], Ruihui Ma[(1)], Feilong Li[(1)], Xiaoli Zhang[(2)], Hua Tian[(3)]

[(1)] *School of Automation, Xi'an Key Laboratory of Advanced Control and Intelligent Processing, Xi'an University of Posts & Telecommunications*
Xi'an, China

[(2)] *Department of Electronic & Information Engineering, Ankang University*
Ankang, Shaanxi, China

[(3)] *Key Laboratory of Ultrasound of Shaanxi Province, School of Physics and Information Technology, Shaanxi Normal University*
Xi'an, China

*Corresponding Author: liguo@xupt.edu.cn

Received July 10, 2025; revised December 25, 2025; accepted January 1, 2026; available online January 15, 2026; version of record March 17, 2026; published issue March 27, 2026.

To reduce the size and enhance the efficiency of cascaded sandwich transducers with conical horns, a novel structural configuration of such transducers is investigated. This transducer incorporates two sets of piezoelectric stacks, enabling two-stage amplification to improve efficiency. An equivalent circuit model of the cascaded sandwich transducer with a conical horn is established, and analytical expressions for key performance parameters, including input impedance, velocity amplification ratio, and resonant characteristics, are systematically derived. Through theoretical and simulation analyses, the dynamic influence of key structural parameters on electromechanical energy conversion efficiency is determined, specifically including the output radius of the second stage, the relative position of the variable cross-sections of two sets of piezoelectric ceramic sandwich structures, and the spacing between the two sets of piezoelectric stacks. Furthermore, a performance optimization strategy based on piezoelectric single-crystal materials is proposed. Numerical simulation results, validated against the theoretical models, reveal the governing principles of piezoelectric material properties on transducer performance. Experimental results demonstrate excellent agreement between the operational characteristics of the optimized transducer and predictions obtained from both theoretical models and finite element simulations. This work provides significant guidance for the optimization of multi-mode transducers and demonstrates promising application potential in high-power ultrasonic fields.

Keywords: cascaded transducer, multi-mode, velocity amplification ratio, finite element analysis.

1. Introduction

In recent years, power ultrasonic technology has demonstrated extensive application prospects across diverse fields, including ultrasonic machining, precision cleaning, underwater acoustics, sonochemistry, food processing, and biodiesel production (Shah, Liu, 2019; Tan *et al.*, 2022; Li *et al.*, 2018b; Pokhrel *et al.*, 2016; Subhedar, Gogate, 2015; Chemat *et al.*, 2011). Particularly, within ultrasonic motor research, piezoelectric transducer-based ultrasonic systems have attracted significant scientific attention (Li *et al.*, 2023b; Roland, 2024; Jiang *et al.*, 2024). As critical components of ultrasonic systems, sandwich piezoelectric ultrasonic transducers exhibit remarkable advantages in electromechanical energy conversion through the piezoelectric effect. These advantages are a simplified structural design, high conversion efficiency, and large vibration amplitude, making them predom-

inant in high-power ultrasonic applications (Lin, 2009; Kuang *et al.*, 2014; Du *et al.*, 2020; Davari *et al.*, 2012). Their applications further extends to piezoelectric nanopositioning systems and robotic manipulators (Su *et al.*, 2018; Jiang *et al.*, 2018; Li *et al.*, 2023a).

To meet escalating demands in high-power applications, research focus has shifted toward optimizing conventional sandwich transducers and developing novel vibration systems. Enhanced radiation coverage and ultrasonic intensity have been achieved through geometric modifications and vibration mode innovations, leading to the proposal of coupled-vibration transducers and mode-conversion composite systems, including longitudinal-torsional, radial-torsional, flexural-torsional, longitudinal-flexural, radial-flexural, and interdigital configurations (Li *et al.*, 2018a; 2023a; Meshkinzar, Al-Jumaily, 2021; Watanabe *et al.*, 1993; Lin *et al.*, 2011; 2013; Tressler *et al.*, 2006; Lin, 2007; Tang *et al.*, 2024; Xu *et al.*, 2019; Hunter *et al.*, 2008). Lin (2017) pioneered the concept of cascaded piezoelectric transducers, where multiple half-wavelength sandwich transducers synergistically amplify input electrical power and ultrasonic intensity. Subsequent work by Lin *et al.* (2018) introduced tunable longitudinal transducers with comprehensive performance characterization. Li *et al.* (2022) conducted a multifrequency analysis of stepped conical transducers, deriving equivalent impedance models and resonance frequency equations through theoretical modeling and experimental validation. Cascaded transducers can operate at different resonant frequencies to meet the requirements of multifrequency modes. This cascaded vibration structure can also double the power and intensity of ultrasonic waves, while the intermediate mass block can assist in heat dissipation. However, systematic investigation of the multi-mode vibration characteristics – crucial for optimizing energy transfer and operational stability – of conical cascaded sandwich transducers remains limited. Specifically, the correlations between the multifrequency performance and key geometric parameters are not well understood, hindering their optimized design for high-power, multi-mode applications.

To address this gap, this study investigates the relationship between performance parameters, geometric dimensions, and piezoelectric materials of a conical cascaded sandwich piezoelectric transducer operating in multifrequency mode. A theoretical analysis model is established by deriving the frequency equations and vibration velocity amplification ratio expression for cascaded transducers using Kirchhoff's law. Keeping the conical amplitude rod structure unchanged, the geometric dimensions of the piezoelectric stack radius near the output end of the amplitude rod and the spatial configuration of the sandwich structure formed by the two piezoelectric stacks are varied, and the piezoelectric material PZT-8 is replaced with a relaxor ferroelectric single crystal (RFSC). The impact of combining PZT-8 with an RFSC on vibration performance are analyzed, and variations in key performance parameters are analyzed using theoretical models and numerical simulations. Based on the theoretical and simulation results, an optimized transducer prototype is manufactured and experimentally tested. The results are in good agreement with the predictions and thus validate the proposed design method. This work provides a practical optimization framework for cascaded transducers with conical horn and offers important guidance for the development of efficient, high-power ultrasonic systems for precision machining, sonochemistry, and other applications.

2. Theoretical analysis

The ultrasonic composite transducer is formed by the longitudinal cascade of two sandwich-type structures, a conical horn, and a prestressed bolt. These two sandwich structures serve as two-stage excitation mechanisms. In the design, the influence of bolt prestress is neglected; consequently, the two sandwich structures and the conical horn can be considered as a solid rod bonded together. Figure 1 illustrates the structural diagram of the ultrasonic transducer, comprising seven components: back metal cylinder I, piezoelectric stack II, middle metal cylinder III, middle metal cylinder IV, piezoelectric stack V, front metal cylinder VI, and conical horn VII. The parameter L_i (i = 1, 2, 3, 4, 5, 6, 7) corresponds to the length of each component, while the parameter R_i (i = 1, 2, 3, 4, 5, 6, 7) corresponds to the cross-sectional radius of each component. N_i (i = 1, 2) represents the electromechanical conversion coefficient of piezoelectric ceramic stack.

The equivalent circuit diagram of the transducer is presented in Fig. 2. Here, V denotes the excitation voltage, I_1 and I_2 represent the currents entering into the two piezoelectric stacks, respectively; v_i (i = 1, 2,

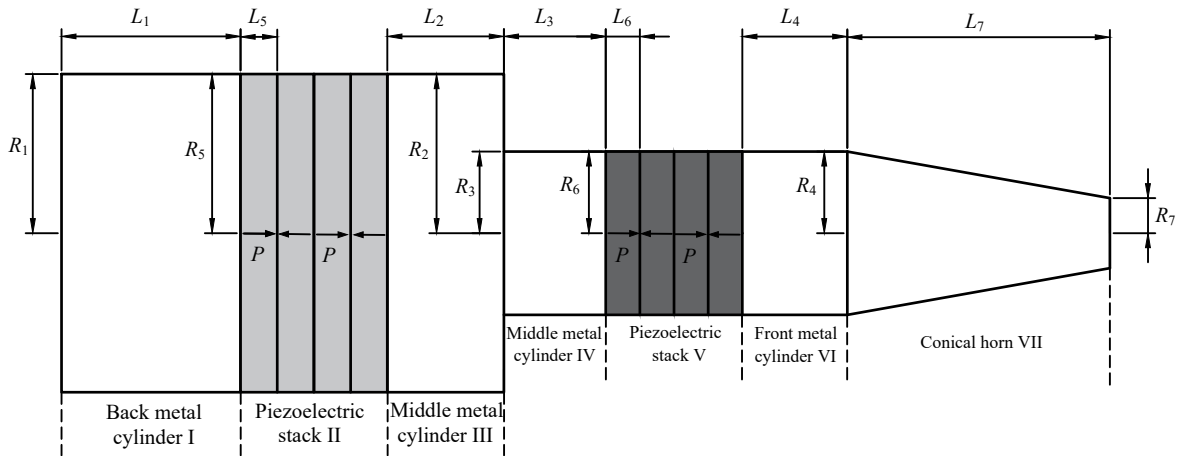

Fig. 1. Structural diagram of the cascaded-excitation longitudinal output system.

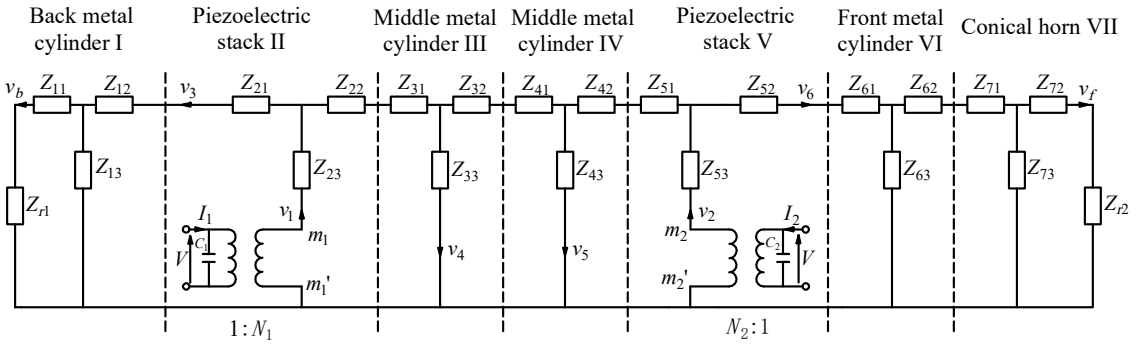

Fig. 2. Equivalent circuit of the cascaded-excitation longitudinal output system.

3, 4, 5, 6) denotes the vibration velocity at each designated section, while v_b and v_f denote the longitudinal vibration velocities at the outer surfaces of the rear metal cylinder and the conical horn, respectively; C_i represents the clamped capacitance of the piezoelectric stacks, N_i is the electromechanical transformation ratio, p is the number of piezoelectric rings, ρ is the material density, E is Young's modulus, k is the wavenumber, and c is the longitudinal wave sound velocity; Z_{i1}, Z_{i2}, Z_{i3} (i = 1, 2, 3, 4, 5, 6, 7) denote the impedances of the metal cylinders and piezoelectric ceramic stacks, respectively, where $Z_{i1} = Z_{i2} = jZ_{0i}\tan\left(\frac{k_i L_i}{2}\right)$, $Z_{i3} = \frac{Z_{0i}}{j\sin(k_i L_i)}$.

Li *et al.* (2024) conducted research on the equivalent circuit of the transducer. From this model, the mechanical impedances Z_{m1} and Z_{m2} between the mechanical terminals m_1, m_1' and m_2, m_2' can be obtained, leading to the derivation of the total equivalent mechanical impedance Z_m:

$$Z_{m1} = Z_{23} + \frac{v_3}{v_1}\left[\frac{(Z_{r1}+Z_{11})Z_{13}}{(Z_{r1}+Z_{11})+Z_{13}} + Z_{12} + Z_{21}\right], \tag{1}$$

$$Z_{m2} = Z_{53} + \frac{v_6}{v_2}\left[\frac{(Z_{71}+Z_{62})(Z_{72}+Z_{73})Z_{32}+Z_{72}Z_{73}}{(Z_{71}+Z_{62}+Z_{63})(Z_{72}+Z_{73})+Z_{72}Z_{73}} + Z_{61} + Z_{52}\right], \tag{2}$$

$$Z_m = \frac{Z_{m1}Z_{m2}}{Z_{m1}(jwC_2Z_{m2}+N_2^2)+Z_{m2}(jwC_1Z_{m1}+N_1^2)}, \tag{3}$$

where $w = 2\pi f$ and f is the frequency.

The resonant frequency f_r is obtained when Z_m approaches zero, and the anti-resonant frequency f_a is calculated when Z_m approaches infinity. The effective electromechanical coupling coefficient is $k_{\text{eff}} = \sqrt{\left(1-\left(\frac{f_r}{f_a}\right)^2\right)}$, and the velocity amplitude magnification ratio is $M = \left|\frac{v_b}{v_f}\right|$.

3. Relationships between performance parameters and geometric dimensions of the cascaded piezoelectric transducer with conical horn

To investigate the influence of the transducers geometric dimensions on its performance, the metal block material is 40Cr steel, while other metal blocks and the conical metal component are made of hard aluminum. The piezoelectric materials employed are PZT-8 and an RFSC. PZT-8 is widely utilized in ultrasonic transducer research due to its advantageous properties, including a high electromechanical coupling coefficient, high mechanical strength, and fast response speed. Compared to PZT-8, the RFSC exhibits higher piezoelectric and dielectric constants along with lower dielectric loss, making it the preferred material for high-precision ultrasonic applications. Their typical characteristic parameters are listed in Table 1. Through theoretical analysis, the function of impedance with respect to frequency can be obtained. By assigning a value to the frequency, the corresponding impedance can be obtained, producing an impedance-frequency curve. From this curve, the resonant and anti-resonant frequencies can be identified, and the electromechanical coupling coefficient can be calculated. By substituting the resonant frequency into the amplification ratio formula, the amplification ratio can be calculated. This theoretical calculation process is implemented using MATLAB. These performance parameters were also obtained through numerical simulation using ANSYS. The model was established in an axisymmetric configuration. The metal components were discretized with PLANE42 elements, a 4-node axisymmetric structural solid element suitable for linear elastic analysis. The piezoelectric ceramic stacks were modeled using PLANE13 elements, a 4-node axisymmetric coupled-field solid element that can directly solve the interaction between electrical and mechanical degrees of freedom. Free meshing with a node size of 0.001 m was applied to each part of the transducer. The effects of pre-tightening bolt stress and structural constraints were neglected during the simulation.

Table 1. Characteristic parameters of the transducer.

Material	ρ [kg/m^3]	E [N/m^2]	v	s_{33}^E [m^2/N]	d_{33} [C/N]	ε_{33}^T [C^2/(N$\cdot$m^2)]	k_{33}
40Cr steel	7840	20.9×10^{10}	0.28	–	–	–	–
Duralumin	2790	7.15×10^{10}	0.34	–	–	–	–
PZT-8	7600	–	–	13.9×10^{-12}	225×10^{-12}	8.84×10^{-9}	0.62
Single crystal	8122	–	–	49×10^{-12}	1285×10^{-12}	42.1×10^{-9}	0.87

3.1. Influence of output radius of the second stage on performance parameters

Using PZT-8 as the piezoelectric material, the initial dimensional parameters of the transducer are: L_1 = 0.02 m, L_2 = L_3 = 0.0075 m, L_4 = 0.021 m, L_5 = L_6 = 0.005 m, L_7 = 0.054 m, R_1 = R_2 = R_3 = R_4 = 0.0255 m, R_5 = R_6 = 0.025 m, R_7 = 0.009 m, p_1 = p_2 = 4, τ_1 = R_2 m. The relationships between the performance parameters and the output radius of the second stage are shown in Fig. 3 to Fig. 5, where the subscripts denote: t for theoretical values, s for simulated values, r for resonance, a for anti-resonance, and the numerical suffix i (i = 1, 2, 3) for the first three longitudinal vibration modes. For example, f_{tr1} refers to the theoretical fundamental resonant frequency, f_{sa2} refers to the simulated second anti-resonant frequency, k_{t1} refers to the theoretical fundamental effective electromechanical coupling coefficient, k_{s2} refers to the simulated second-order effective electromechanical coupling coefficient, M_{t1} refers to the theoretical fundamental velocity amplitude, and M_{s2} refers to the simulated second-order velocity amplitude magnification.

Figure 3 shows that as the τ_1 increases, the fundamental longitudinal vibration resonant and anti-resonant frequencies both increase, while the second-order longitudinal vibration resonant and anti-resonant frequencies decrease. For the third-order longitudinal vibration, the theoretical resonance frequency increases, and the simulated resonance frequency first increases and then decreases, but the changes are very small, whereas the anti-resonant frequency decreases. In Fig. 4, the fundamental longitudinal vibration electromechanical coupling coefficient increases, whereas the effective electromechanical coupling coefficients of the second- and third-order longitudinal vibrations exhibit decreasing trends. Within smaller radius ranges, both fundamental and second-order longitudinal vibrations maintain relatively large effective electromechanical coupling coefficients, with the simulated third-order coupling coefficient showing a distinct minimum. Figure 5 indicates that the fundamental longitudinal

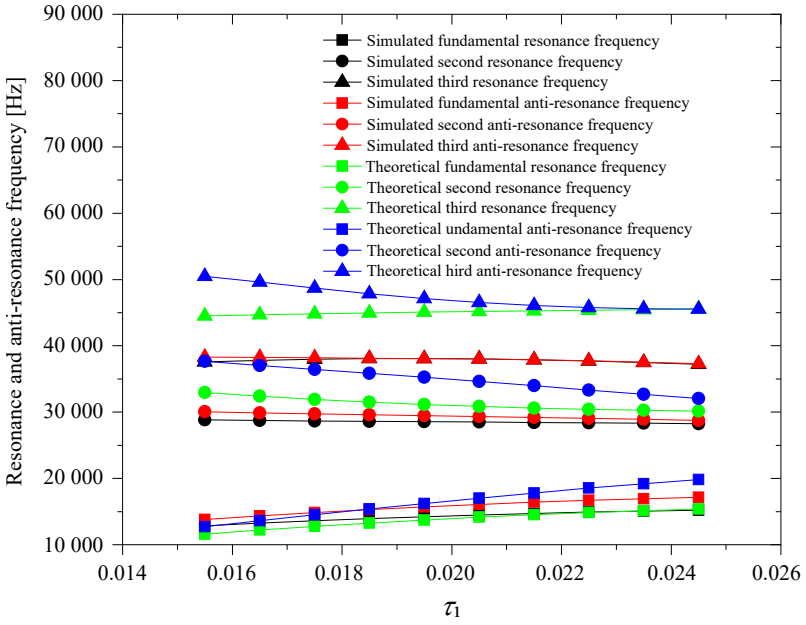

Fig. 3. Relationship between the resonance and anti-resonance frequency and τ_1.

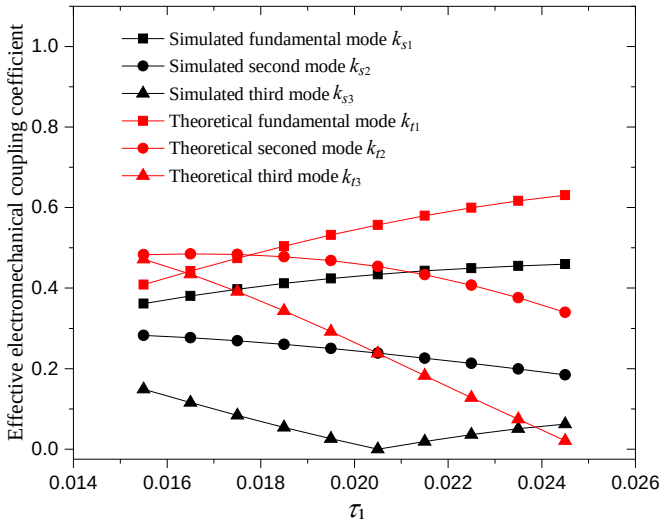

Fig. 4. Relationship between the effective electromechanical coupling coefficient and τ_1.

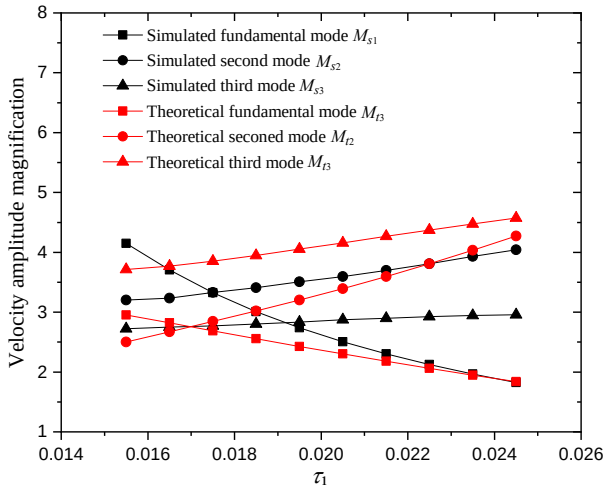

Fig. 5. Relationship between the velocity amplitude magnification and τ_1.

vibration velocity amplification ratio decreases with increasing τ_1, while the second- and third-order velocity amplification ratios increase proportionally. When τ_1 reaches approximately 20.5 mm, the transducer simultaneously achieves large effective electromechanical coupling coefficients and velocity amplification ratios for the first two longitudinal vibration modes, establishing this value as the optimized radius for the right-side sandwich-type piezoelectric stack. Therefore, $R_3 = R_4 = 0.0205$ m and $R_6 = 0.02$ m were selected as the optimized dimensional parameters.

3.2. Influence of the relative position of the variable cross-section of two sets of piezoelectric ceramic sandwich structures on performance parameters

As described in the previous section, the radii of the metal blocks and piezoelectric ceramics are kept unchanged. The lengths L_2 and L_3 are varied, but the total length L_2 and L_3 remains constant. The initial dimensional parameters of the transducer are: $L_1 = 0.02$ m, $L_2 = L_3 = 0.0075$ m, $L_4 = 0.021$ m, $L_5 = L_6 = 0.005$ m, $L_7 = 0.054$ m, $R_1 = R_2 = 0.0255$ m, $R_3 = R_4 = 0.0205$ m, $R_5 = 0.025$ m, $R_6 = 0.02$ m, $R_7 = 0.009$ m, $p_1 = p_2 = 4$, and $\tau_2 = L_2/L_3$. The relationships between the resonance frequency, anti-resonance frequency, effective electromechanical coupling coefficient, and velocity amplification ratio with respect to τ_2 are shown in Fig. 6 to Fig. 8.

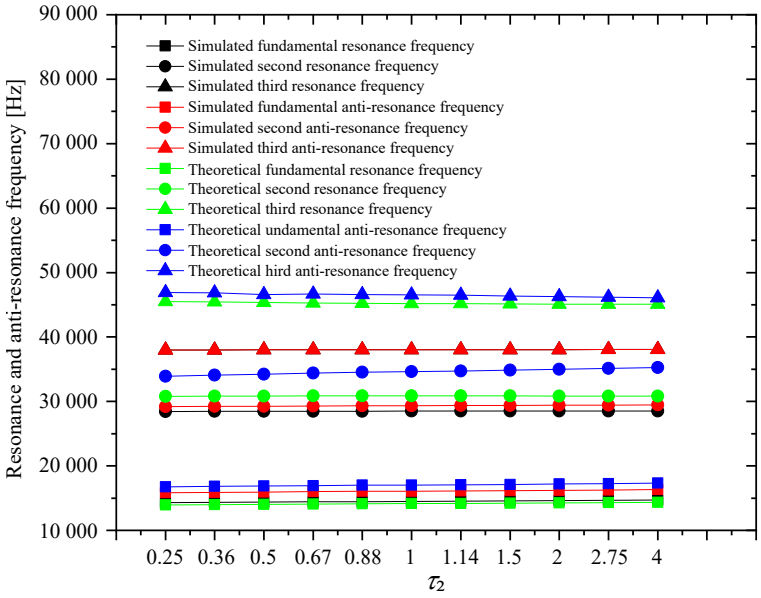

Fig. 6. Relationship between the resonance and anti-resonance frequency and τ_2.

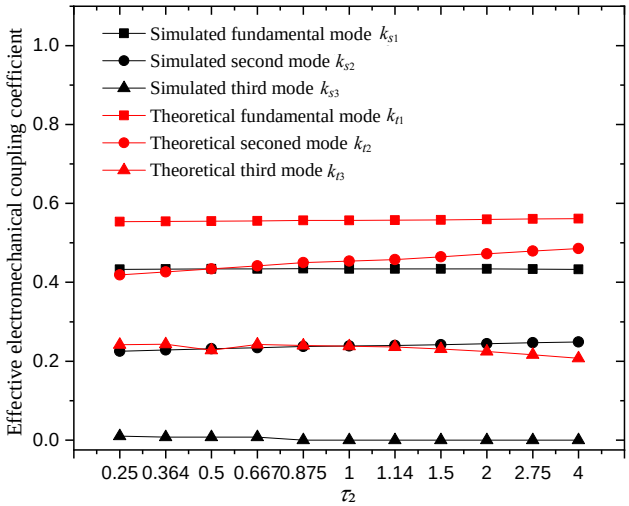

Fig. 7. Relationship between the effective electromechanical coupling coefficient and τ_2.

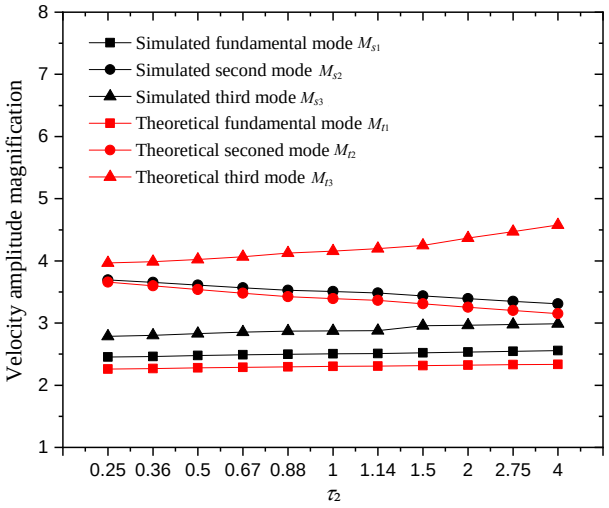

Fig. 8. Relationship between the velocity amplitude magnification and τ_2.

Figure 6 demonstrates that as τ_2 increases, the resonant and anti-resonant frequencies of the first three longitudinal vibration modes all exhibit gradual increases. In Fig. 7, the electromechanical coupling coefficients of the first- and second-order longitudinal vibrations show slow increases with τ_2, while the third-order longitudinal vibration electromechanical coupling coefficient gradually decreases. The velocity amplification ratios of the first- and third-order longitudinal vibrations rise slowly with τ_2. Figure 8 reveals a gradual decrease in the second-order longitudinal vibration velocity amplification ratio as τ_2 increases. Overall, variations in the relative position of the variable cross-sections in the two sandwich-type piezoelectric stacks exert minimal influence on the resonant/anti-resonant frequencies, electromechanical coupling coefficients, and velocity amplification ratios. The optimal relative position is determined as $\tau_2 = 1$ for the variable cross-sections in the two sandwich-type piezoelectric stack structures.

3.3. Influence of the spacing between two groups of piezoelectric ceramics on performance parameters

As discussed in the preceding section, while maintaining the other structural dimensions of the vibration system constant, the spacing between the two sets of piezoelectric ceramics was varied. This spacing corresponds to the length of the middle metal cylinders III and IV. The length changes of these two metal cylinder were identical, while the total length of the transducer remained unchanged. Consequently, the lengths of the back metal cylinder I and the front metal cylinder VI were adjusted correspondingly to accommodate the changes in the middle metal cylinder III and IV. The initial dimensional parameters of the transducer are: $L_1 = 0.02$ m, $L_2 = L_3 = 0.0075$ m, $L_4 = 0.021$ m, $L_5 = L_6 = 0.005$ m, $L_7 = 0.054$ m, $R_1 = R_2 = 0.0255$ m, $R_3 = R_4 = 0.0205$ m, $R_5 = 0.025$ m, $R_6 = 0.02$ m, $R_7 = 0.009$ m, $p_1 = p_2 = 4$, and $\tau_3 = L_2 + L_3$ m. The relationships between the resonance frequency, anti-resonance frequency, effective electromechanical coupling coefficient, velocity amplification ratio with respect to τ_3 are shown in Fig. 9 to Fig. 11.

Figure 9 indicates that, as τ_3 increases, the resonant and anti-resonant frequencies of the first three longitudinal vibration modes exhibit gradual decreases. In Fig. 10, the effective electromechanical coupling coefficients of the first- and second-order longitudinal vibrations decrease with increasing τ_3, while the third-order coupling coefficient initially decreases and then increases. Figure 11 demonstrates that the velocity amplification ratios for all three longitudinal vibration modes decreases as τ_3 increases, with the first- and second-order modes exhibiting smaller reductions compared to the third-order mode. Both theoretical and simulation results indicate that a smaller τ_3 between the two piezoelectric stacks enhances the effective electromechanical coupling coefficients and the velocity amplification ratios for the first two vibration modes. Considering manufacturing and assembly constraints, as well as the vibrational coupling intensity between structural components, the piezoelectric ceramic spacing is optimized to 10 mm.

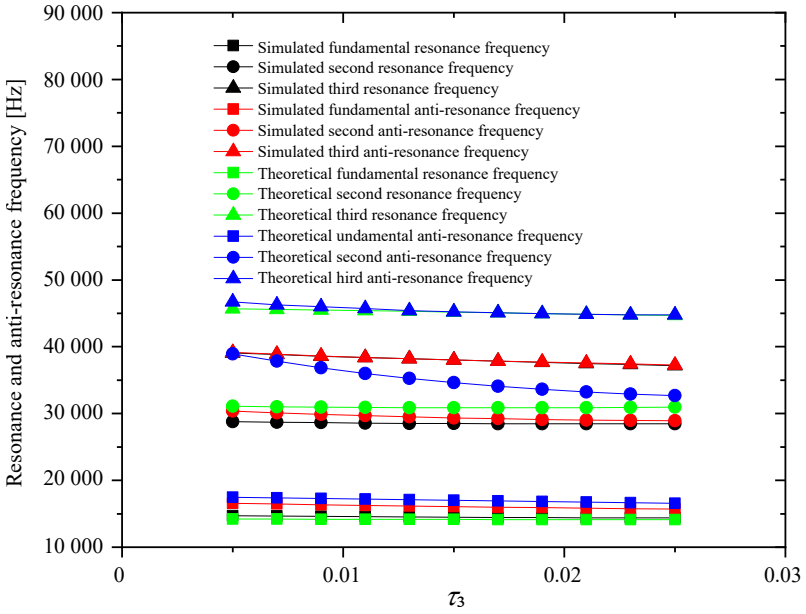

Fig. 9. Relationship between the resonance and anti-resonance frequency and τ_3.

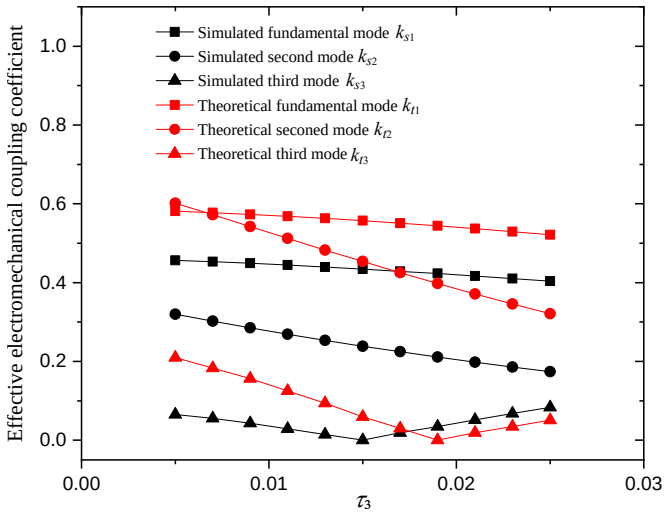

Fig. 10. Relationship between the effective electromechanical coupling coefficient and τ_3.

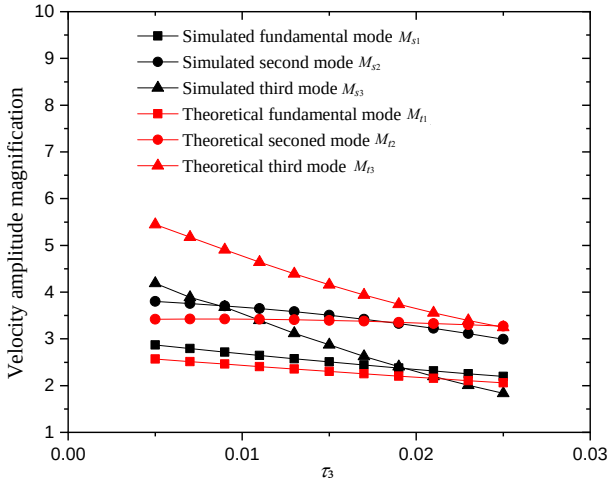

Fig. 11. Relationship between the velocity amplitude magnification and τ_3.

3.4. Influence of piezoelectric materials on performance parameters

Replacing piezoelectric ceramics with RFSCs alters the transducer performance, as quantified by theoretical and simulated parameters listed in Table 2. The parameters f_{tri}, f_{tai}, f_{sri}, f_{sai}, k_{ti}, k_{si}, M_{ti}, and M_{si} represent the theoretical/simulated resonance/anti-resonance frequencies, effective electromechanical coupling coefficients, and velocity amplitude amplification ratios, respectively. Here, $i = 1$, $i = 2$, and $i = 3$ denote configurations with bilateral piezoelectric ceramics, a left-side piezoelectric ceramic/right-side RFSC, and bilateral RFSCs, respectively. Table 2 demonstrates that replacing the right-side piezoelectric ceramic with an RFSC increases the first- and third-order electromechanical coupling coefficients but reduces the second-order coupling coefficients, while the amplification ratios exhibit negligible variation. In contrast, substituting both sides with RFSCs induces a pronounced upward trend in all electromechanical coupling coefficients, accompanied by reduced amplification ratios for the fundamental and second-order modes and an increased third-order amplification ratio.

Theoretical and simulated results for bilateral piezoelectric ceramics.

Table 2. Theoretical and simulated results for different piezoelectric material configurations.

Theoretical and simulated results for bilateral piezoelectric ceramics.								
Mode	f_{tr1} [Hz]	f_{ta1} [Hz]	f_{sr1} [Hz]	f_{sa1} [Hz]	k_{t1}	k_{s1}	M_{t1}	M_{s1}
Fundamental	14 177	17 265	14 585	16 305	0.571	0.447	2.43	2.68
Second	30 939	36 411	28 606	29 769	0.527	0.277	3.34	3.68
Third	45 453	45 883	38 481	38 506	0.137	0.036	4.77	3.54
Theoretical and simulated results for the left-side piezoelectric ceramic/right-side RFSC.								
Mode	f_{tr2} [Hz]	f_{ta2} [Hz]	f_{sr2} [Hz]	f_{sa2} [Hz]	k_{t2}	k_{s2}	M_{t2}	M_{s2}
Fundamental	12 509	18 578	11 113	15 271	0.739	0.686	2.68	2.69
Second	33 799	37 198	27 042	27 298	0.418	0.137	3.18	3.37
Third	43 554	44 996	30 577	31 366	0.251	0.223	4.78	3.56
Theoretical and simulated results for the bilateral RFSCs.								
Mode	f_{tr3} [Hz]	f_{ta3} [Hz]	f_{sr3} [Hz]	f_{sa3} [Hz]	k_{t3}	k_{s3}	M_{t3}	M_{s3}
Fundamental	8953	14 259	10 046	14 704	0.778	0.730	1.88	1.89
Second	20 824	31 883	20 615	21 767	0.757	0.321	1.66	1.77
Third	32 740	33 469	29 647	30 690	0.208	0.258	5.72	4.63

Figure 12 to Fig. 14 display the harmonic displacement responses from the front to the rear radiation surfaces of transducers with three piezoelectric ceramic-RFSC configurations across the first three vibration modes. When both sides employ piezoelectric ceramics, symmetrical displacement distributions emerge, with lower amplitudes in the fundamental mode, while higher-order modes exhibit progressively amplified vibrations and potential multi-peak displacement patterns. For the asymmetric configuration (left-side piezoelectric ceramic/right-side RFSC), the RFSC demonstrates localized amplitude enhancement in the second- and third- modes due to its superior mechanical compliance. However, the ceramic's rigidity restricts vibration energy transfer to the rear surface, resulting in insignificant improvement in the amplification ratio compared with the bilateral ceramic configurations. The bilateral RFSC achieves the maximum overall vibration amplitudes, as the high material compliance promotes efficient energy propagation to the rear surface, generating substantial posterior displacement. Concurrently, reduced wave reflection and increased energy dissipation at the front surface diminish its vibration amplitude, ultimately causing significant degradation of the amplification ratio.

In summary, replacing the right-side piezoelectric ceramic with RFSCs predominantly enhances the electromechanical coupling coefficients while minimally affecting the amplification ratios, enabling transducers to achieve both high coupling coefficients and velocity amplification at low-order modes. Complete substitution with bilateral RFSCs further optimizes electromechanical coupling performance, demonstrating the material's potential for advanced transducer applications. In practical manufacturing processes, the size of RFSCs is usually designed to be smaller. The size optimization presented in this study makes it possible to apply RFSCs in transducers. Compared with conventional piezoelectric ceramics, the performance can be comparable or even superior. In reality, the material combination can be chosen according to the specific application needs.

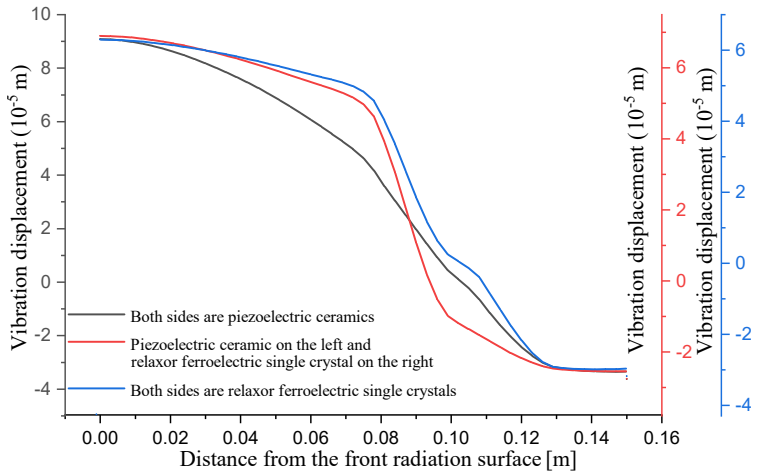

Fig. 12. Fundamental harmonic displacement response curve.

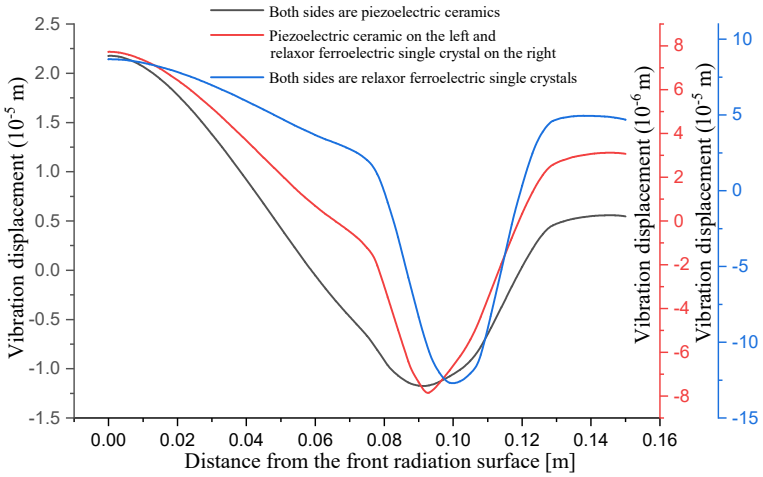

Fig. 13. Second-order harmonic displacement response curve.

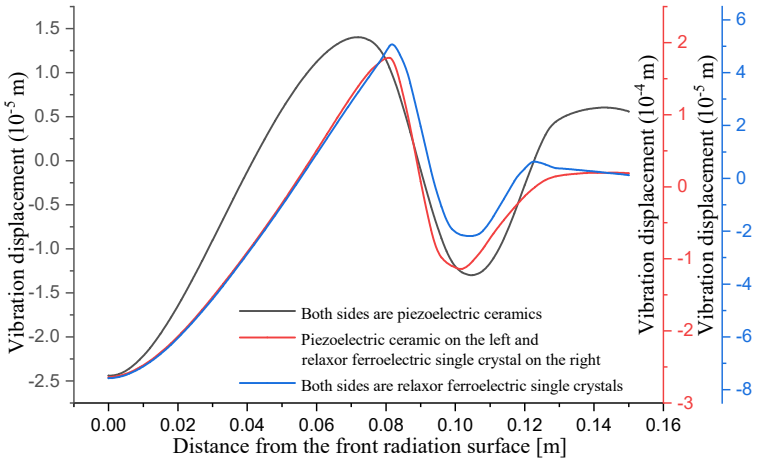

Fig. 14. Third-order harmonic displacement response curve.

4. Experiment

Based on the transducer dimensions designed in Sec. 3, a physical prototype was fabricated and tested. The corresponding structural dimensions are listed in Table 3, while Fig. 15. First three mode shapes illustrates the mode shapes of the transducer under three distinct vibration modes. In this transducer, the capacitances of the left

Table 3. Structural dimensions of the cascaded piezoelectric transducer [mm].

L_1	L_2	L_3	L_4	L_{01}	L_{02}	L_7	R_1	R_2	R_{01}	R_{02}	R_7
22.5	5	5	23.5	5	5	54	25.5	20.5	25	20	9

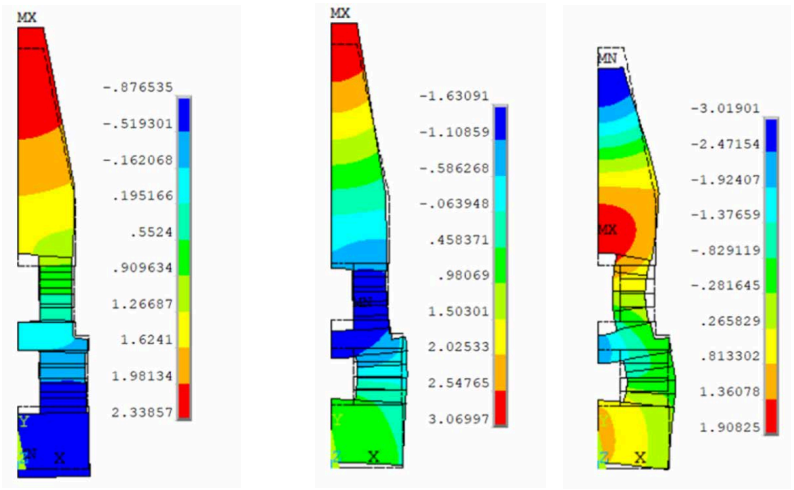

Fig. 15. First three mode shapes of the transducer.

piezoelectric ceramic are 3.414 nF, 3.409 nF, 3.418 nF, and 3.406 nF, respectively, and the capacitances of the right piezoelectric ceramic are 1.606 nF, 1.625 nF, 1.608 nF, and 1.635 nF, respectively. The total capacitance of the transducer is 20.01 nF, indicating good electrical connectivity.

Reactance-frequency responses were acquired using a precision impedance analyzer (E4990A) under 1 V excitation over the range of 10 kHz to 45 kHz. The experimental setup and measured reactance-frequency characteristics are presented in Fig. 16 and Fig. 17. Notably, spectral peaks correspond to anti-resonance states while troughs indicate resonance conditions, with the first three resonance points matching the aforementioned vibration modes. Table 4 provides comparative resonance/anti-resonance frequency data obtained using different analytical approaches.

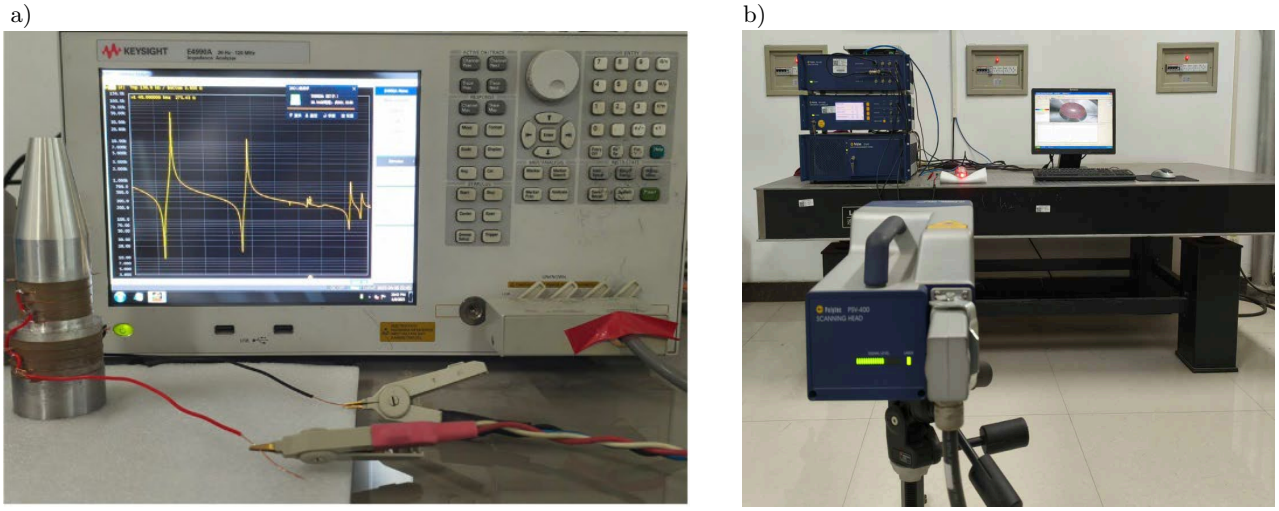

Fig. 16. a) Measuring electrical impedance-frequency response of the transducer by using the E4990A precision impedance analyzer, b) measuring vibration mode of the transducer by using the Polytec scanning vibrometer.

The vibration velocities at the metal block end face and conical output terminal of the transducer were measured using a Polytec laser vibrometer. Figure 16 shows the experimental setup, Fig. 17 illustrates the experimental electrical impedance-frequency response curve and experimental longitudinal vibration displacement

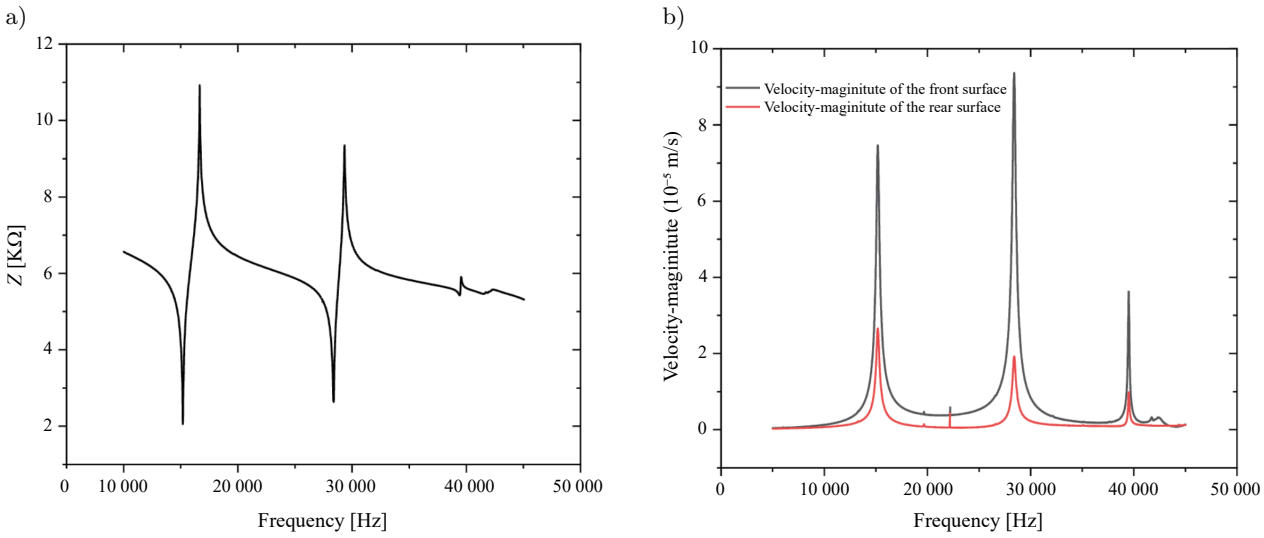

Fig. 17. a) Experimental electrical impedance-frequency response curve, b) experimental longitudinal vibration displacement frequency-response results.

Table 4. Theoretical, simulated, and measured frequencies of the multi-frequency mode transducer.

Mode	f_{tr} [Hz]	f_{ta} [Hz]	f_{sr} [Hz]	f_{sa} [Hz]	f_{mr} [Hz]	f_{ma} [Hz]
Fundamental	14 177	17 265	14 585	16 305	15 187	16 660
Second	30 939	36 411	28 606	29 769	28 367	29 343
Third	45 453	45 883	38 481	38 506	39 418	39 549

frequency-response results. The longitudinal vibration displacement distributions are presented in Fig. 18. The first two longitudinal vibration modes exhibit relatively pure characteristics, while the third-order demonstrates coupling vibration effects caused by the larger transverse dimension at the rear end. Nevertheless, the front end maintains satisfactory longitudinal vibration output. The effective electromechanical coupling coefficients and velocity amplification ratios were calculated using $k_{\text{eff}} = \sqrt{\left(1 - \left(\frac{f_r}{f_a}\right)^2\right)}$ and $M = \left|\frac{v_b}{v_f}\right|$, with comparative results from theoretical, simulated, and experimental approaches listed in Table 5, k_t, k_s, k_m, and M_t, M_s, M_m denote the theoretical, simulated, and measured values, respectively.

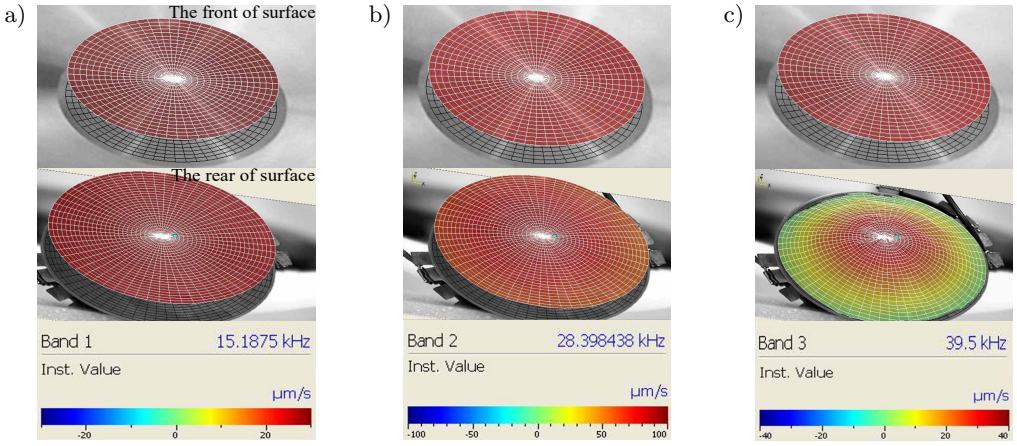

Fig. 18. Longitudinal vibration displacement distributions on the front and rear radiation surfaces of the transducer: a) fundamental mode, b) second-order, c) third-order.

As shown in Table 4, the theoretical, simulated, and experimental values for the first two resonant/anti-resonant frequencies show excellent agreement. However, a larger discrepancy is observed for the third-order

Table 5. Theoretical, simulated, and measured effective electromechanical coupling coefficient and velocity amplitude magnifications of the multi-frequency mode transducer.

Mode	k_t	k_s	k_m	M_t	M_s	M_m
Fundamental	0.571	0.447	0.412	2.403	2.68	2.87
Second	0.527	0.277	0.256	3.34	3.68	4.86
Third	0.137	0.036	0.081	4.77	3.54	3.68

frequency, where the theoretical value deviates significantly from both the simulated and experimental results. This discrepancy arises because the theoretical model is based on 1D analysis, which neglects the influence of transverse vibrations. As the mode order increases, the impact of transverse coupling effects becomes progressively more significant, leading to increased error. Furthermore, discrepancies between the simulated and experimental values exist due to inevitable deviations of the actual material parameters from their nominal values, combined with the neglect of bolt stress effects in the simulation.

As shown in Table 5, the simulated and experimental values of the effective electromechanical coupling coefficient exhibit good agreement, while the theoretical values are consistently higher. This discrepancy arises because the theoretical model neglects dielectric losses and assumes idealized fixed boundary conditions. The experimental velocity amplification ratio for the second-order is significantly higher than both theoretical and simulated values. This occurs because the measured resonant frequency is lower than theoretically predicted, indicating that the actual system stiffness is lower than anticipated. This measured frequency likely approaches the transducer's true optimal resonant point, where vibration phase matching between the piezoelectric ceramic stack and metal blocks is improved, resulting in enhanced amplification efficiency. Conversely, the theoretical amplification ratio for the third-order substantially exceeds both simulated and experimental values. This overestimation stems from the theoretical assumption of perfectly rigid metal blocks, whereas at higher frequencies, material compliance and micro-slip at connections become significant, leading to an overestimation of amplification performance. The remaining amplification ratios show good consistency across all three methods.

5. Conclusions

This paper investigated the multi-modal vibration characteristics of a longitudinal cascaded sandwich transducer incorporating a conical horn. Through theoretical and simulation analyses, the influence of key structural parameters on performance was determined, specifically the output radius of the second-stage, the relative position of the variable cross-section of two sets of piezoelectric ceramic sandwich structures, and the spacing between the two sets of piezoelectric ceramics. Optimal transducer dimensions were derived and subsequently validated experimentally. Furthermore, a hybrid configuration combining PZT-8 ceramics with RFSCs was proposed, revealing the impact of piezoelectric material selection on performance metrics. The established optimization methodology provides guidance for multi-mode transducer design, while the optimized transducer demonstrates promising application potential in high-power ultrasonic systems. The principal conclusions are as follows:

1. Reducing the output radius of the second-stage facilitates the concurrent maintenance of substantial effective electromechanical coupling coefficients for the fundamental and second-order longitudinal vibrations, while the third-order effective electromechanical coupling coefficient simulations reach minimal values within smaller radius ranges. This configuration simultaneously enhances fundamental vibration velocity amplification ratios while diminishing higher-order responses.
2. The relative positions of the two variable cross-section piezoelectric stacks demonstrated negligible influence on operational parameters.
3. Minimizing the spacing between the two piezoelectric stacks improves both effective electromechanical coupling coefficients and velocity amplification ratios in primary vibration modes, representing a critical design consideration for practical implementations.
4. Replacing conventional ceramics with RFSCs in the right-side configurations yields enhanced effective electromechanical coupling coefficients without compromising velocity amplification. Bilateral substitution

further increases effective electromechanical coupling coefficients at the expense of reduced amplification ratios, offering flexible material selection strategies for application-specific requirements. These findings establish a methodological framework for performance-adaptive transducer design in high-intensity ultrasonic applications.

Fundings

This work was supported by the National Natural Science Foundation of China (grant nos. 12104369 and 12174004), the Key Research and Development Project of Shaanxi Province in China (no. 2025SF-YBXM-470).

Conflict of interests

The authors declare that they have no known competing financial interests or personal relationships that could have appeared to influence the work reported in this paper.

Authors' contributions

Guo Li conceptualized the study, supervised the research and acquired funding. Peiyu Tan performed the theoretical analysis, numerical simulations, and experimental measurements, and wrote the original draft. Ruihui Ma and Feilong Li assisted in simulations and data validation. Xiaoli Zhang contributed to resources and manuscript review. Hua Tian provided laboratory support and administered the project. All authors reviewed and approved the final manuscript.

References

1. Chemat F., Zill-e-Huma, Khan M.K. (2011), Applications of ultrasound in food technology: Processing, preservation and extraction, *Ultrasonics Sonochemistry*, **18**(4): 813–835, https://doi.org/10.1016/j.ultsonch.2010.11.023.
2. Davari P., Ghasemi N., Zare F., O'Shea P., Ghosh A. (2012), Improving the efficiency of high power piezoelectric transducers for industrial applications, *IET Science, Measurement & Technology*, **6**(4): 213–221, https://doi.org/10.1049/iet-smt.2011.0209.
3. Du Y.D., Xu L., Zhou G.P. (2020), Vibration characteristics of two-dimensional orthogonal composite sandwich piezoelectric circular transducer [in Chinese], *SCIENTIA SINICA Physica, Mechanica & Astronomica*, **51**(11): 115311, https://doi.org/10.1360/SSPMA-2020-0417.
4. Hunter G., Lucas M., Watson I., Parton R. (2008), A radial mode ultrasonic horn for the inactivation of *Escherichia coli* K12, *Ultrasonics Sonochemistry*, **15**(2): 101–109, https://doi.org/10.1016/j.ultsonch.2006.12.017.
5. Jiang C.R., Cheng S.N., Shen Z., Jin L. (2024), Design and analysis of impedance matching for a radial standing wave piezoelectric ultrasonic motor, *Review of Scientific Instruments*, **95**(1): 015003, https://doi.org/10.1063/5.0180662.
6. Jiang Z., Wang L., Jin J.M. (2018), A novel robotic arm driven by sandwich piezoelectric transducers, *Ultrasonics*, **84**: 373–381, https://doi.org/10.1016/j.ultras.2017.11.019.
7. Kuang Y., Jin Y., Cochran S., Huang Z. (2014), Resonance tracking and vibration stablilization for high power ultrasonic transducers, *Ultrasonics*, **54**(1): 187–194, https://doi.org/10.1016/j.ultras.2013.07.001.
8. Li F.-M., Liu S.-Q., Xu L., Zhang H.-D., Zeng X.-M., Chen Z.-J. (2023a), Open-slit circular tube piezoelectric ultrasonic transducer with longitudinal bending mode conversion [in Chinese], *SCIENTIA SINICA Physica, Mechanica & Astronomica*, **53**(11): 114311, https://doi.org/10.1360/SSPMA-2023-0233.
9. Li G. *et al.* (2024), Investigation of a cascaded piezoelectric transducer with cone horn for multi-mode power ultrasound application, *Physica Scripta*, **99**: 105997, https://doi.org/10.1088/1402-4896/ad6d05.
10. Li G., Gong J.H., Wang T., Qiu C.R., Xu Z. (2018a), Study on the broadband piezoelectric ceramic transducer based on radial enhanced composite structure, *Ceramics International*, **44**(Supplement 1): S250–S253, https://doi.org/10.1016/j.ceramint.2018.08.101.
11. Li G., Qu J.S., Xu L., Zhang X.L., Gao X.Y. (2022), Study on multi-frequency characteristics of a longitudinal ultrasonic transducer with stepped horn, *Ultrasonics*, **121**: 106683, https://doi.org/10.1016/j.ultras.2022.106683.

12. Li G., Xu Z., Gong J.H., Li F., Liu Y.B. (2018b), Modeling and experiment of a small size dual mode transducer for underwater acoustic communication and detection, *Acta Acustica*, **104**(6): 947–955, https://doi.org/10.3813/AAA.919260.

13. Li J.Q., Zheng J.D., Pan H., Tong J., Feng K., Ni Q. (2023b), Two-dimensional composite multi-scale time–frequency reverse dispersion entropy-based fault diagnosis for rolling bearing, *Nonlinear Dynamics*, **111**: 7525–7546, https://doi.org/10.1007/s11071-023-08250-y.

14. Lin S.Y. (2007), Radial vibration of the composite ultrasonic transducer of piezoelectric and metal rings, *IEEE Transactions on Ultrasonics, Ferroelectrics, and Frequency Control*, **54**(6): 1276–1280, https://doi.org/10.1109/TUFFC.2007.381.

15. Lin S.Y. (2009), Analysis of multifrequency Langevin composite ultrasonic transducers, *IEEE Transactions on Ultrasonics, Ferroelectrics, and Frequency Control*, **56**(9): 1990–1998, https://doi.org/10.1109/TUFFC.2009.1275.

16. Lin S.Y. (2017), A new type of cascaded high intensity piezoelectric ultrasonic transducers [in Chinese], *Journal of Shaanxi Normal University (Natural Science Edition)*, **45**(06): 22–28, https://doi.org/10.15983/j.cnki.jsnu.2017.06.261.

17. Lin S.Y., Fu Z.Q., Zhang X.L., Wang Y., Hu J. (2013), Radially sandwiched cylindrical piezoelectric transducer, *Smart Materials and Structures*, **22**: 015005, https://doi.org/10.1088/0964-1726/22/1/015005.

18. Lin S.Y., Guo H., Xu J. (2018), Actively adjustable step-type ultrasonic horns in longitudinal vibration, *Journal of Sound and Vibration*, **419**: 367–379, https://doi.org/10.1016/j.jsv.2018.01.033.

19. Lin S.Y., Xu L., Hu W.X. (2011), A new type of high power composite ultrasonic transducer, *Journal of Sound and Vibration*, **330**(7): 1419–1431, https://doi.org/10.1016/j.jsv.2010.10.009.

20. Liu S.Q., Yao Y., Lin S.Y. (2009), Radial-torsional vibration mode of disc-type piezoelectric transducer, *Journal of Mechanical Engineering*, **45**(06): 176–180, https://doi.org/10.3901/JME.2009.06.176.

21. Meshkinzar A., Al-Jumaily A.M. (2021), Vibration and acoustic radiation characteristics of cylindrical piezoelectric transducers with circumferential steps, *Journal of Sound and Vibration*, **511**: 116346, https://doi.org/10.1016/j.jsv.2021.116346.

22. Pokhrel N., Vabbina P.K., Pala N. (2016), Sonochemistry: Science and engineering, *Ultrasonics Sonochemistry*, **29**: 104–128, https://doi.org/10.1016/j.ultsonch.2015.07.023.

23. Roland R. (2024), Improving output performance of the ultrasonic multicell piezoelectric motor by development the multi-rotor structure, *IEEE Access*, **12**: 32080–32088, https://doi.org/10.1109/ACCESS.2024.3370560.

24. Shah U.H., Liu X. (2019), Ultrasonic resistance welding of TRIP-780 steel, *Journal of Materials Processing Technology*, **274**: 116287, https://doi.org/10.1016/j.jmatprotec.2019.116287.

25. Su Q., Liu Y.X., Wang L., Deng J., Li H. (2018), A three-dimensional piezoelectric nanopositioner using a sandwich transducer, *Ceramics International*, **44**(Supplement 1): S108–S111, https://doi.org/10.1016/j.ceramint.2018.08.226.

26. Subhedar P.B., Gogate P.R. (2015), Ultrasound assisted intensification of biodiesel production using enzymatic interesterification, *Ultrasonics Sonochemistry*, **29**: 67–75, https://doi.org/10.1016/j.ultsonch.2015.09.006.

27. Tan W.X., Tan K.W., Tan K.L. (2022), Developing high intensity ultrasonic cleaning (HIUC) for post-processing additively manufactured metal components, *Ultrasonics*, **126**: 106829, https://doi.org/10.1016/j.ultras.2022.106829.

28. Tang Y.F., Chen C., Tian H., Lin S. (2024), Radial vibration analysis for piezoceramic shell-stacked spherical transducer with thick walls, *Smart Materials and Structures*, **33**: 035002, https://doi.org/10.1088/1361-665X/ad1e8f.

29. Tressler J.F., Howarth T.R., Huang D. (2006), A comparison of the underwater acoustic performance of single crystal versus piezoelectric ceramic based "cymbal" projectors, *The Journal of the Acoustical Society of America*, **119**(2): 879–889, https://doi.org/10.1121/1.2150153.

30. Watanabe Y., Tsuda Y., Mori E. (1993), A longitudinal-flexural complex-mode ultrasonic high-power transducer system with one-dimensional construction, *Japanese Journal of Applied Physics*, **32**: 2430, https://doi.org/10.1143/JJAP.32.2430.

31. Xu L., Qiu X.J., Zhou J.C., Li F.M., Zhang H.D., Wang Y.B. (2019), A 2D dual-mode composite ultrasonic transducer excited by a single piezoceramic stack, *Smart Materials and Structures*, **28**: 025017, https://doi.org/10.1088/1361-665X/aaf275.